

Long-Lived Topological Flatband Excitons in Semiconductor Moiré Heterostructures: A Bosonic Kane-Mele Model Platform

Ming Xie,^{1,*} Mohammad Hafezi,² and Sankar Das Sarma^{1,2}

¹*Condensed Matter Theory Center, Department of Physics,
University of Maryland, College Park, Maryland 20742, USA*

²*Joint Quantum Institute, Department of Physics,
University of Maryland, College Park, Maryland 20742, USA*

(Dated: October 2, 2024)

Moiré superlattices based on two-dimensional transition metal dichalcogenides (TMDs) have emerged as a highly versatile and fruitful platform for exploring correlated topological electronic phases. One of the most remarkable examples is the recently discovered fractional quantum anomalous Hall effect (FQAHE) under zero magnetic field. Here we propose a minimal structure that hosts long-lived excitons—a ubiquitous bosonic excitation in TMD semiconductors—with narrow topological bosonic bands. The nontrivial exciton topology originates from hybridization of moiré interlayer excitons and is tunable by controlling twist angle and electric field. At small twist angle, the lowest exciton bands are isolated from higher energy bands and provide a solid-state realization of the bosonic Kane-Mele model with topological flatbands, which could potentially support the bosonic version of FQAHE.

Introduction—Owing to their narrow bandwidths and intertwined electronic wave functions, moiré superlattices formed from overlaying two-dimensional transition metal dichalcogenide (TMD) semiconductors have become a unique crossroad where strong electron correlations and nontrivial topology meet, under unprecedented controllability. In TMD superlattices where band topology is trivial, a plethora of strongly correlated phenomena, such as Mott insulators, generalized Wigner crystals, and metal-insulator transitions, have been identified [1–12]. Recently, in TMD superlattices featuring topological bands, experimental studies observed correlated phases with nontrivial topological characteristics [13–21], including both integer and fractional quantum anomalous Hall states. The latter, also referred to as fractional Chern insulators, are observed for the first time in experiments after being proposed for over a decade [22–26]. These observations establish TMD moiré superlattices as promising candidates for solid-state fermionic quantum simulations.

The drastic influence of the long-period moiré pattern extends to excitons—tightly bound electron-hole pair excitations—in TMD moiré superlattices, rendering their localization on moiré lattices [27–38]. Remarkably, recent experiments discovered a correlated incompressible state of excitons [39–44], or a bosonic Mott insulator, in TMD moiré heterobilayers, breaking new ground for exploring many-body states of bosons. The moiré modulation in these superlattices leads to localized excitons seating on a triangular lattice with strong on-site interactions, effectively simulating the Bose-Hubbard model. The emergence of localized bosonic lattices can be understood as the formation of trivial excitonic moiré bands with narrow bandwidths. One intriguing question arises: Is it possible to form topological moiré bands for excitons, thereby paving the way to achieve bosonic corre-

lated topological phases, such as bosonic fractional Chern insulators?

It was understood that excitons in the $+K$ and $-K$ valleys of TMD monolayers have nonzero Berry curvatures due to valley-momentum coupling induced by exchange interactions [50–53]. Based on this, Wu and coworkers [34] showed that, when such intralayer exciton is subjected to a periodic moiré potential, the resulting low-energy moiré exciton bands can acquire a definite Chern number, provided an effective valley Zeeman field is included. However, one critical issue that remains unaddressed in this scenario is the short lifetime of excitons, which is detrimental for experimental realization of many-body states of excitons. Intralayer excitons are known to have large optical dipole moment responsible for their short recombination lifetime; they decay rapidly before a quasiequilibrium population of excitons can be established. The fact that the strength of the valley-momentum coupling is proportional to the optical dipole moment places topology and long lifetime at odds with each other.

In this Letter, we propose a minimal TMD moiré heterostructure capable of supporting excitons that are both long-lived and topological. It is based on interlayer moiré excitons whose optical dipole moments nearly vanish due to layer separation of their constituent electron and hole. The topology of the exciton moiré bands originates from spatially varying hybridization of interlayer excitons situated in different layers of the moiré heterostructure. This mechanism does not involve the exchange-induced exciton Berry curvature, thereby avoiding the conflict between topology and long lifetime. We develop an effective bosonic continuum model for the interlayer moiré excitons. The valley-projected exciton band structure features a rich set of bosonic topological bands with opposite Chern numbers for opposite valley pseudospins.

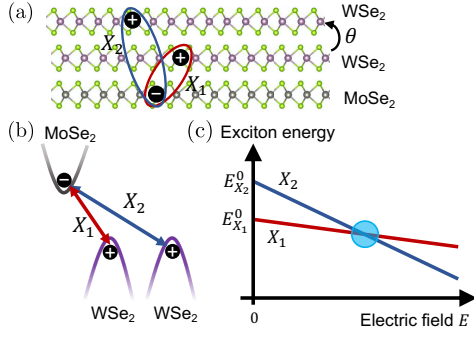


FIG. 1. (a) Schematic illustration of the proposed moiré heterostructure. The WSe₂ layers are twisted relative to each other by an angle θ while the MoSe₂ layer is aligned with the middle WSe₂ layer. (b) The band diagram hosting the two low-energy interlayer excitons, X_1 and X_2 , illustrated in (a). (c) Energy of the X_1 and X_2 excitons as a function of the vertical electric field.

We find that, as the twist angle is varied, the bandwidth of the lowest exciton band exhibits a minimum at a “magic” angle. At small twist angles, the pair of isolated lowest-energy exciton bands provides a first solid-state realization of the bosonic Kane-Mele model with nearly flat topological bands.

Moiré heterostructure—The proposed structure consists of a twisted MX_2 (tMX_2) homobilayer stacked on top of another $M'X_2$ monolayer, with rotation alignment between the interfacial MX_2 and $M'X_2$ layers, as illustrated in Fig. 1(a), where M, M' represent different transition metal atoms, W or Mo, and X represents a S, Se, or Te atom. We have chosen TMD layers with a common chalcogen element (X), for their negligible mismatch in lattice constant [45], to avoid unimportant complications due to the formation of a second moiré pattern at the heterointerface. (Our theory also applies, in this regard, if a thin h BN spacer is added.) As will become clear below, it is the tMX_2 that provides the moiré-modulated hybridization critical to our theory.

In this work, we focus on the $tWSe_2$ /MoSe₂ heterostructure as an example [49], which features a type-II band alignment with a momentum-direct interlayer band gap between the conduction band of the MoSe₂ and the valence bands of the $tWSe_2$ at the $\pm K$ valleys [Fig. 1(b)]. The lowest-energy excitons are the intravalley interlayer excitons formed by electrons in the MoSe₂ layer and holes in the middle and top WSe₂ layers, labeled as X_1 and X_2 , respectively [shown in Fig. 1(a)]. Because of their different electron-hole vertical separations, X_1 and X_2 excitons have different binding energies. Their energies, $E_{X_l} = E_{X_l}^0 - eV_b/2$ (with $e > 0$), can be tuned by a perpendicular electric field E as shown in Fig. 1(c), where $l = 1, 2$, $V_b = 2\epsilon E d$ is the bias potential across the trilayer, d is interlayer spacing, and $E_{X_l}^0$ is the exciton energy at $E = 0$. As we demonstrate below, interesting physics occurs when X_1 and X_2 are close in en-

ergy, and hybridize with each other [highlighted in cyan in Fig. 1(c)].

The electron-hole two-body problem in the moiré superlattice can be simplified, taking advantage of the facts that the exciton binding energy (~ 100 meV) is much larger than the interlayer hybridization strength (~ 10 – 20 meV), and that the binding energy variation in the superlattice potential is generally smaller than the band gap variation [36, 38]. This allows us to treat the exciton problem and the effect of the superlattice separately in a two-step process. We start by solving the Bethe-Salpeter equations (BSEs) [34, 36, 52] in the absence of the moiré potential and interlayer hybridization:

$$(E_{\tau,c,\mathbf{k}+\alpha_c\mathbf{Q}} - E_{\tau,v,l,\mathbf{k}-\alpha_v\mathbf{Q}})A_{S,l,\mathbf{Q}}^\tau(\mathbf{k}) + \sum_{\mathbf{k}'} \langle \tau l \mathbf{k} \mathbf{Q} | V | \tau l \mathbf{k}' \mathbf{Q} \rangle A_{S,l,\mathbf{Q}}^\tau(\mathbf{k}') = \mathcal{E}_{S,l}^\tau(\mathbf{Q}) A_{S,l,\mathbf{Q}}^\tau(\mathbf{k}), \quad (1)$$

where \mathbf{Q} and \mathbf{k} are the center-of-mass (c.m.) and relative momentum of the electron-hole state, $|\tau l \mathbf{k} \mathbf{Q}\rangle \equiv \hat{c}_{\tau c \mathbf{k} + \alpha_c \mathbf{Q}}^\dagger \hat{c}_{\tau v l \mathbf{k} - \alpha_v \mathbf{Q}} |0\rangle$. $\hat{c}^\dagger(\hat{c})$ is the electron creation (annihilation) operator, and $|0\rangle$ is the charge neutrality state. $\alpha_{c(v)} = m_{c(v)}^*/M$ with $M = m_c^* + m_v^*$ the exciton effective mass. $\tau = \pm K$ is the valley index, and $l = 1, 2$ denotes the middle ($l = 1$) and the top ($l = 2$) WSe₂ layers. S is the exciton band index. We adopted the usual convention that \mathbf{k} is measured from the $\pm K$ point of each layer. $\langle \tau l \mathbf{k} \mathbf{Q} | V | \tau l \mathbf{k}' \mathbf{Q} \rangle$ represents the direct interlayer Coulomb interaction matrix (see Supplemental Material (SM) for details [54]).

The lowest-energy solution ($S = 0$) of each BSE is the interlayer exciton state X_l with energy $\mathcal{E}_l^\tau(\mathbf{Q})$ and wave function:

$$|X_l(\mathbf{Q})\rangle_\tau = \sum_{\mathbf{k}} A_{l,\mathbf{Q}}^\tau(\mathbf{k}) \hat{c}_{\tau c \mathbf{k} + \alpha_c \mathbf{Q}}^\dagger \hat{c}_{\tau v l \mathbf{k} - \alpha_v \mathbf{Q}} |0\rangle. \quad (2)$$

The internal wave function $A_{l,\mathbf{Q}}^\tau(\mathbf{k})$ is nearly independent of \mathbf{Q} and isotropic in \mathbf{k} , reminiscent of the $1s$ exciton wave function. (We have dropped the S index for convenience.) $\mathcal{E}_l^\tau(\mathbf{Q}) \approx E_{X_l} + \hbar^2 \mathbf{Q}^2 / M$ at small \mathbf{Q} . The energy difference $\Delta E^0 \equiv E_{X_2}^0 - E_{X_1}^0$ is about 50 meV. We note that a more accurate treatment of the exciton problem could be achieved using the *ab initio* GW-BSE approach [52, 57], which, however, falls outside the focus and scope of this work.

Exciton moiré Hamiltonian—We now derive a continuum model Hamiltonian for the interlayer excitons, taking into account the effect of the moiré superlattice modulation and interlayer hybridization. Since the valence bands are situated in the $tWSe_2$ superlattice, the hole component of the excitons experience a moiré potential modulation [34]. The moiré potential takes the form [58, 59]

$$U_l(\mathbf{r}) = 2V \sum_{i=1,3,5} \cos(\mathbf{g}_i \cdot \mathbf{r} + s_{i,l}\phi), \quad (3)$$

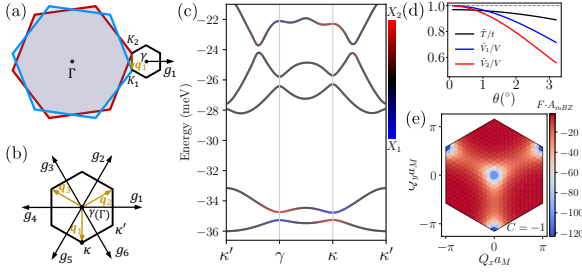


FIG. 2. (a) Rotated Brillouin zones of the middle (cyan) and top (red) WSe₂ layers and the moiré Brillouin zone (black) of the tWSe₂. (b) Exciton moiré Brillouin zone with its center (γ point) set at the origin Γ of momentum space. (c) Band structure moiré excitons at $\theta = 1.5^\circ$ and $eV_b - 2\Delta E_0 = 4.2$ meV. Blue (red) line color indicates the fraction of the X_1 (X_2) component. (d) \tilde{V}_1/V and \tilde{T}/t as a function of the twist angle. (e) Berry curvature of the lowest exciton band with Chern number $C_0 = -1$.

where V and ϕ are the amplitude and phase parameters, respectively, and $s_{i,l} = (-1)^{i+l-1}$. $\mathbf{g}_1 = 4\pi/\sqrt{3}a_M(1,0)$ and $\mathbf{g}_i = (\hat{\mathcal{R}}_{\pi/3})^{i-1}\mathbf{g}_1$ are moiré reciprocal lattice vectors where $\hat{\mathcal{R}}_{\pi/3}$ is counterclockwise rotation around the z axis by $\pi/3$ [Fig. 2(a)]. By Fourier transforming $U_l(\mathbf{r})$ and projecting it to the exciton basis in Eq. (2), we obtain the exciton moiré potential:

$$U_{l,\mathbf{Q},\mathbf{Q}'}^+ = -\tilde{V}_l \sum_{i=1}^6 \exp(is_{i,l}\phi) \delta_{\mathbf{Q}-\mathbf{g}_i,\mathbf{Q}'}, \quad (4)$$

where the superscript “+” indicates valley, and the minus sign reflects that excitons experience an opposite sign of moiré potential compared to that of the valence electrons. The amplitude $\tilde{V}_l = V \sum_{\mathbf{k}} A_{l,0}^+(\mathbf{k}) A_{l,0}^+(\mathbf{k} + \alpha_c \mathbf{g}_1)$ depends on the overlap of exciton internal wave functions with a relative shift $\alpha_c \mathbf{g}_1$ (see SM [54] for details) and decreases with increasing twist angle, as shown in Fig. 2(d). The delta function ensures the conservation of exciton c.m. momentum \mathbf{Q} up to a moiré reciprocal vector.

The X_1 and X_2 excitons hybridize with each other via the interlayer hybridization between the valence bands of the tWSe₂, which varies periodically in real space leading to nontrivial layer pseudospin winding [59–63]. In the lowest-order harmonic approximation, it takes the form for valley $+K$

$$T^+(\mathbf{r}) = t \sum_n e^{i\mathbf{q}_n \cdot \mathbf{r}}, \quad (5)$$

where t is the tunneling strength. $\mathbf{q}_1 = \mathbf{K}_1 - \mathbf{K}_2$ is the momentum shift between the K points in the two WSe₂ layers and \mathbf{q}_n is related to \mathbf{q}_1 by threefold rotation $\mathbf{q}_n = (\hat{\mathcal{R}}_{2\pi/3})^{n-1}\mathbf{q}_1$ [Fig. 2(a)]. Similar to Eq. 4, we obtain the hybridization Hamiltonian:

$$\mathcal{T}_{\mathbf{Q},\mathbf{Q}'}^+ = t \sum_{n=1}^3 \sum_{\mathbf{k}} A_{1,\mathbf{Q}}^{+*}(\mathbf{k}) A_{2,\mathbf{Q}'}^+(\mathbf{k} - \alpha_c \mathbf{q}_n) \delta_{\mathbf{Q}+\mathbf{q}_n,\mathbf{Q}'}, \quad (6)$$

where the amplitude for the three hopping processes $\tilde{T}_n \equiv t \sum_{\mathbf{k}} A_{1,\mathbf{Q}}^{+*}(\mathbf{k}) A_{2,\mathbf{Q}+\mathbf{q}_n}^+(\mathbf{k} - \alpha_c \mathbf{q}_n)$, are equal $\tilde{T}_1 = \tilde{T}_2 = \tilde{T}_3 \equiv \tilde{T}$ because of the C_3 symmetry (around the z axis). Similar to \tilde{V}_1/V , \tilde{T}/t decreases monotonically with increasing θ [shown in Fig. 2(d)]. It should be emphasized that the c.m. momentum of X_2 exciton is measured from $\boldsymbol{\kappa} = \mathbf{K}_1 - \mathbf{K}_2$ instead of from γ for the X_1 exciton.

Combining Eqs. (4) and (6), we arrive at the full exciton moiré Hamiltonian (for valley $\tau = +K$) in the basis $\{|X_1\rangle_+, |X_2\rangle_+\}$:

$$\mathcal{H}_{\mathbf{Q},\mathbf{Q}'}^+ = \begin{pmatrix} \mathcal{E}_1(\mathbf{Q})\delta_{\mathbf{Q},\mathbf{Q}'} + U_{1,\mathbf{Q},\mathbf{Q}'}^+ & \mathcal{T}_{\mathbf{Q},\mathbf{Q}'}^+ \\ [\mathcal{T}^+]_{\mathbf{Q},\mathbf{Q}'}^\dagger & \mathcal{E}_2(\mathbf{Q})\delta_{\mathbf{Q},\mathbf{Q}'} + U_{2,\mathbf{Q},\mathbf{Q}'}^+ \end{pmatrix}, \quad (7)$$

which respects the C_3 symmetry and is related to \mathcal{H}^- by time-reversal symmetry \mathcal{T} . We choose the exciton moiré Brillouin zone (mBZ) whose center (γ point) sits at the origin of c.m. momentum Γ , as illustrated in Fig. 2(b), and numerically diagonalize \mathcal{H}^\pm to obtain the exciton moiré band structure [54].

Exciton topological flatbands—The valley-projected ($\tau = +K$) exciton moiré band structure is shown in Fig. 2(c) at a representative twist angle $\theta = 1.5^\circ$ and $eV_b - 2\Delta E_0 = 4.2$ meV. The band structure features two narrow low-energy bands isolated from higher-energy bands. A gap opens up between the two as a result of the hybridization between the X_1 and X_2 excitons. The Berry curvature of the lowest band, illustrated in Fig. 2(e), exhibit strong amplitudes at high symmetry points γ and κ , reminiscent of a band inversion that occurs at these points (see SM [54]). The Chern numbers of the two lowest bands are $C_0 = -1$ and $C_1 = 1$, indicating that a pair of time-reversal symmetry protected bosonic helical edge states exist inside their gap.

Upon varying twist angle and displacement field, the exciton bands display a rich topological phase diagram as illustrated in Fig. 3(a). As eV_b is tuned closer to $2\Delta E^0$, the band inversion between the first and second moiré bands occurs, resulting in a topological transition from the trivial phase with $(C_0, C_1) = (0, 0)$ to the topological phase with $(C_0, C_1) = (-1, +1)$. The gap between the two lowest bands Δ_{01} closes at the transition point as shown in Fig. 3(b). For small twist angle $\theta < 1.4^\circ$, the displacement field range for the inverted region is narrow because of the small bandwidths. As θ increases, the $n = 1$ band intersects the higher ($n = 2$) band at around $\theta = 2^\circ$ [where Δ_{12} vanishes as shown in Fig. 3(c)], leading to a change in the Chern number, from $C_1 = +1$ to $C_1 = -1$, while C_0 remains unchanged. This intersection also leads to the transition from the $(0, 0)$ to $(0, -2)$ phase at large $|eV_b - 2\Delta E^0|$. Interestingly, the bandwidth W_0 of the lowest band exhibits a minimum close to zero at around $\theta_m = 2^\circ$, marking the first emergence of a “magic angle” for a bosonic topological band. Exciton-exciton

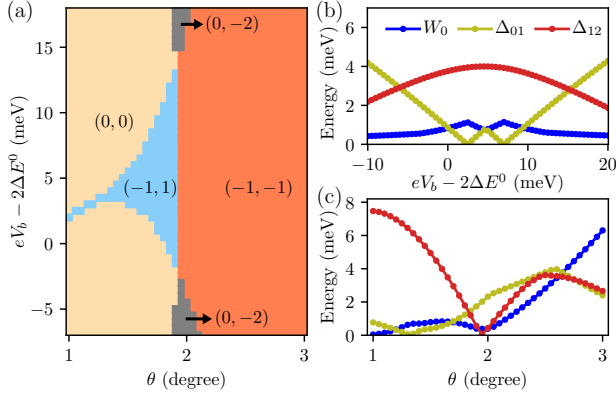


FIG. 3. (a) Topological phase diagram of the moiré exciton bands. The numbers in the parentheses are (C_0, C_1) , the Chern number of the two lowest bands. (b) Bandwidth and energy gap as a function of eV_b at $\theta = 1.6^\circ$. W_0 is the bandwidth of the lowest ($n = 0$) moiré band. Δ_{01} (Δ_{12}) is the global gap between the $n = 0$ and 1 ($n = 1$ and 2) bands. (c) Bandwidth and energy gaps as a function of θ at fixed $eV_b - 2\Delta E^0 = 5$ meV.

interactions, estimated to be around 30–80 meV [39–44, 64], dominate over the bandwidth at small twist angles.

Bosonic Kane-Mele model—The topology and real space density [54] of the two lowest exciton moiré bands indicate that they can be described by an effective Kane-Mele lattice model with two orbitals (or sublattices) in each unit cell. To confirm this, we construct Wannier states for the two lowest bands in regions where their total Chern number is zero; outside these regions, additional bands and thereby Wannier orbitals must be included. The Wannier functions (for valley $+K$) at $\mathbf{R} = 0$ are given by

$$|W_\alpha\rangle = \frac{1}{\sqrt{N}} \sum_{n=0,1} \sum_{\mathbf{Q}} F_{\alpha,n,\mathbf{Q}}^n |\Psi_{n,\mathbf{Q}}\rangle \quad (8)$$

for $\alpha = 1, 2$. $F_{\mathbf{Q}}$ is a unitary matrix for fixing the gauge of the wave function $|\Psi_{n,\mathbf{Q}}\rangle$. We obtain $F_{\mathbf{Q}}$ by requiring that $\sum_n F_{\alpha,n,\mathbf{Q}}^n |\Psi_{n,\mathbf{Q}}\rangle$ is maximally polarized to its $X_{l=\alpha}$ component and is real at its center (where its amplitude peaks) in real space. (See details in SM [54] and also Ref. [65].) Figures 4(c)-4(f) plot the X_1 and X_2 components of $W_\alpha(\mathbf{r}) = [W_{\alpha,1}(\mathbf{r}), W_{\alpha,2}(\mathbf{r})]^T$ for site $\mathbf{R} = 0$. $W_\alpha(\mathbf{r})$ has dominant weight in its $W_{\alpha,\alpha}(\mathbf{r})$ component and is centered around $\mathbf{r} = \mathbf{t}_\alpha$, where $\mathbf{t}_1 = (1/\sqrt{3}, 0)a_M$ and $\mathbf{t}_2 = (2/\sqrt{3}, 0)a_M$ correspond to the XM and MX positions, respectively, in the moiré superlattice. We construct the bosonic tight-binding model for the honeycomb lattice formed by the W_1 and W_2 orbitals as shown in Fig. 4(b). The effective lattice Hamiltonian, keeping the

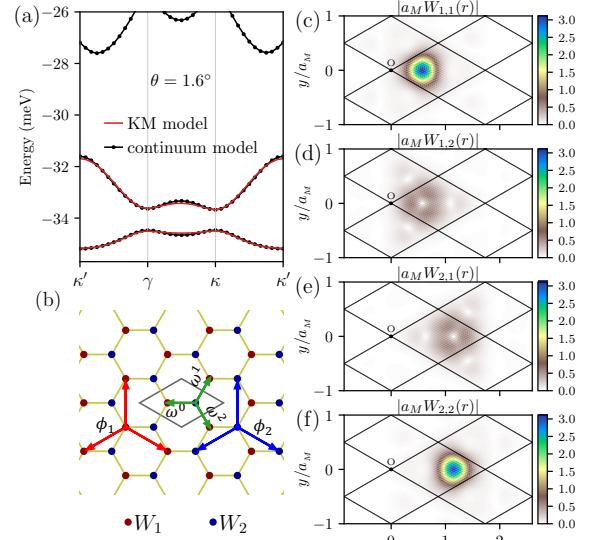


FIG. 4. (a) Bosonic Kane-Mele tight-binding model dispersion (red solid line) compared with the continuum model bands with $\theta = 1.6^\circ$ and $eV_b - 2\Delta E^0 = 4.5$ meV. (b) Schematic illustration of the Kane-Mele tight-binding model (for valley $\tau = +K$) with nearest- (NN) and next-nearest-neighbor (NNN) hoppings. ω^n and ϕ_α represent the phase of the NN and NNN hopping processes, respectively, where $\omega = e^{i2\pi/3}$. The black diamond marks a real space moiré unit cell. (c)-(f) Amplitudes of the Wannier orbitals in real space. $W_{\alpha,l}$ is the X_l component of the W_α orbital at the moiré site $\mathbf{R} = 0$. The black grids mark the moiré unit cells.

nearest and next-nearest hopping terms, takes the form

$$\mathcal{H}_{eff}^{+K} = - \sum_{\alpha,i} \sum_{m=1}^3 t_\alpha^{(2)} e^{i\phi_\alpha} \hat{b}_{\alpha,\mathbf{R}_i + \mathbf{a}_m}^\dagger \hat{b}_{\alpha,\mathbf{R}_i} - \sum_{\alpha,i} \sum_{m=1}^3 t_\alpha^{(1)} e^{i\omega^{m-1}} \hat{b}_{1,\mathbf{R}_i + \delta_m}^\dagger \hat{b}_{2,\mathbf{R}_i} + H.c. \quad (9)$$

where $\hat{b}_{\alpha,\mathbf{R}_i}^\dagger$ is the bosonic creation operator for the W_{α,\mathbf{R}_i} state. $\mathbf{a}_1 = (\sqrt{3}/2, -1/2)a_M$ and $\mathbf{a}_m = (\hat{\mathcal{R}}_{2\pi/3})^{m-1} \mathbf{a}_1$ are real lattice vectors, and $\delta_m = \{\mathbf{0}, -\mathbf{a}_3, \mathbf{a}_1\}$. The first term is the intrasublattice hopping with amplitude $t_\alpha^{(2)}$ and phase ϕ_α . $\phi_1 = 0$ and $\phi_2 = \boldsymbol{\kappa} \cdot \mathbf{a}_1$ in the limit of zero interlayer hybridization, $T = 0$, and gradually deviates from these values as T is increased. The second term is the nearest interorbital hopping term where $\omega = e^{i2\pi/3}$. The bond-dependent phase seemingly breaks C_3 symmetry but, in fact, does not. This is because $|W_1\rangle$ and $|W_2\rangle$ transform differently under C_3 , $C_3|W_{1,\mathbf{R}}\rangle = |W_{1,\mathbf{R}'}\rangle$, and $C_3|W_{2,\mathbf{R}}\rangle = \omega|W_{2,\mathbf{R}'}\rangle$ with $\mathbf{R}' + \mathbf{t}_\alpha = \hat{\mathcal{R}}_{2\pi/3}(\mathbf{R} + \mathbf{t}_\alpha)$ (See SM [54]). \mathcal{H}_{eff}^{+K} is a generalized version of the Haldane Hamiltonian [66] and, together with the \mathcal{H}_{eff}^{-K} , forms the Kane-Mele (KM) model [67]. The dispersion of the effective KM model agrees well with the continuum model

band structure as illustrated in Fig. 4(a), confirming the accuracy of truncating at the NNN hoppings.

Discussions and outlook—The $tMX_2/M'X_2$ moiré heterostructure we propose realizes topological excitons with extended lifetimes, crucial for exploring strongly correlated many-body bosonic phases, and establishes a new mechanism for inducing exciton topology that has not been explored before. Most excitingly, it provides a promising route for realizing the first solid-state-based platform for the bosonic Kane-Mele model, which features topological flatbands and is, therefore, capable of simulating strongly correlated topological bosons. It has been predicted that, in a Haldane-Bose-Hubbard model with topological flatbands, fractional quantum anomalous Hall states emerge at even denominator filling factors $\nu = 1/2$ and $1/4$ [68]. Interestingly, convincing numerical evidence of a stable bosonic non-Abelian quantum Hall state (without Landau level) is also found in such system at $\nu = 1$ [69]. Given the unprecedented tunability of TMD moiré superlattice, our proposal elevates the potential for uncovering these correlated topological phases, especially the non-Abelian quantum anomalous Hall state.

A hallmark of topological exciton bands is the presence of helical edge states inside the noninteracting topological gap, which can be probed by local scanning probes [70] and optical reflection measurements [71] with moiré-scale spatial resolution. In the FQAHE phases predicted at finite exciton densities, bulk incompressibility manifests as jumps in the spectral peak energy upon increasing density. While the nature of their edge states remains largely unexplored, we anticipate several characteristics inferred from the FQHE case [72–76], including algebraically decaying correlation functions, chiral edge channels, and fractionalization. The first two can be detected optically through spatial correlation and diffusion measurements. Electrical generation and control of excitons [77–80] also enable exciton electric and thermal transport measurements, potentially revealing the fractional nature of the edge states.

Acknowledgments—The authors acknowledge helpful discussions with Allan MacDonald, You Zhou, Jiabin Yu, Beini Gao, and Lifu Zhang. This work was supported by Laboratory for Physical Sciences. M. H. acknowledges support from the Army Research Office (ARO) under Grant No. W911NF-20-1-0232.

* mingxie@umd.edu

- [1] Y. Tang, L. Li, T. Li, Y. Xu, S. Liu, K. Barmak, K. Watanabe, T. Taniguchi, A. H. MacDonald, J. Shan, and K. F. Mak, *Nature (London)* **579**, 353 (2020).
- [2] E. C. Regan, D. Wang, C. Jin, M. I. B. Utama, B. Gao, X. Wei, S. Zhao, W. Zhao, Z. Zhang, K. Yumigeta, M. Blei, J. D. Carlström, K. Watanabe, T. Taniguchi, S. Tongay, M. Crommie, A. Zettl, and F. Wang, *Nature (London)* **579**, 359 (2020).
- [3] Y. Xu, S. Liu, D. A. Rhodes, K. Watanabe, T. Taniguchi, J. Hone, V. Elser, K. F. Mak, and J. Shan, *Nature (London)* **587**, 214 (2020).
- [4] L. Wang, E.-M. Shih, A. Ghiotto, L. Xian, D. A. Rhodes, C. Tan, M. Claassen, D. M. Kennes, Y. Bai, B. Kim, K. Watanabe, T. Taniguchi, X. Zhu, J. Hone, A. Rubio, A. N. Pasupathy, and C. R. Dean, *Nat. Mater.* **19**, 861 (2020).
- [5] Z. Zhang, Y. Wang, K. Watanabe, T. Taniguchi, K. Ueno, E. Tutuc, and B. J. LeRoy, *Nat. Phys.* **16**, 1093 (2020).
- [6] C. Jin, Z. Tao, T. Li, Y. Xu, Y. Tang, J. Zhu, S. Liu, K. Watanabe, T. Taniguchi, J. C. Hone, L. Fu, J. Shan, and K. F. Mak, *Nat. Mater.* **20**, 940 (2021).
- [7] T. Li, S. Jiang, L. Li, Y. Zhang, K. Kang, J. Zhu, K. Watanabe, T. Taniguchi, D. Chowdhury, L. Fu, J. Shan, and K. F. Mak, *Nature (London)* **597**, 350 (2021).
- [8] S. Shabani, D. Halbertal, W. Wu, M. Chen, S. Liu, J. Hone, W. Yao, D. N. Basov, X. Zhu, and A. N. Pasupathy, *Nat. Phys.* **17**, 720 (2021).
- [9] X. Huang, T. Wang, S. Miao, C. Wang, Z. Li, Z. Lian, T. Taniguchi, K. Watanabe, S. Okamoto, D. Xiao, S.-F. Shi, and Y.-T. Cui, *Nat. Phys.* **17**, 715 (2021).
- [10] Y. Tang, J. Gu, S. Liu, K. Watanabe, T. Taniguchi, J. C. Hone, K. F. Mak, and J. Shan, *Nat. Commun.* **13**, 4271 (2022).
- [11] A. Ghiotto, E.-M. Shih, G. S. S. G. Pereira, D. A. Rhodes, B. Kim, J. Zang, A. J. Millis, K. Watanabe, T. Taniguchi, J. C. Hone, L. Wang, C. R. Dean, and A. N. Pasupathy, *Nature (London)* **597**, 345 (2021).
- [12] W. Zhao, B. Shen, Z. Tao, Z. Han, K. Kang, K. Watanabe, T. Taniguchi, K. F. Mak, and J. Shan, *Nature (London)* **616**, 61 (2023).
- [13] T. Li, S. Jiang, B. Shen, Y. Zhang, L. Li, T. Devakul, K. Watanabe, T. Taniguchi, L. Fu, J. Shan, and K. F. Mak, *Nature (London)* **600**, 641 (2021).
- [14] J. Cai, E. Anderson, C. Wang, X. Zhang, X. Liu, W. Holtzmann, Y. Zhang, F. Fan, T. Taniguchi, K. Watanabe, Y. Ran, T. Cao, L. Fu, D. Xiao, W. Yao, and X. Xu, *Nature (London)* **622**, 63 (2023).
- [15] Y. Zeng, Z. Xia, K. Kang, J. Zhu, P. Knüppel, C. Vaswani, K. Watanabe, T. Taniguchi, K. Fai Mak, and J. Shan, *Nature (London)* **622**, 69 (2023).
- [16] H. Park, J. Cai, E. Anderson, Y. Zhang, J. Zhu, X. Liu, C. Wang, W. Holtzmann, C. Hu, Z. Liu, T. Taniguchi, K. Watanabe, J.-H. Chu, T. Cao, L. Fu, W. Yao, C.-Z. Chang, D. Cobden, D. Xiao, and X. Xu, *Nature (London)* **622**, 74 (2023).
- [17] F. Xu, Z. Sun, T. Jia, C. Liu, C. Xu, C. Li, Y. Gu, K. Watanabe, T. Taniguchi, B. Tong, J. Jia, Z. Shi, S. Jiang, Y. Zhang, X. Liu, and T. Li, *Phys. Rev. X* **13**, 031037 (2023).
- [18] B. A. Foutty, C. R. Kometter, T. Devakul, A. P. Reddy, K. Watanabe, T. Taniguchi, L. Fu, and B. E. Feldman, *Science* **384**, 343 (2024).
- [19] Z. Tao, B. Shen, S. Jiang, T. Li, L. Li, L. Ma, W. Zhao, J. Hu, K. Pistunova, K. Watanabe, T. Taniguchi, T. F. Heinz, K. Fai Mak, and J. Shan, *Phys. Rev. X* **14**, 011004 (2024).
- [20] K. Kang, B. Shen, Y. Qiu, K. Watanabe, T. Taniguchi, J. Shan, and K. F. Mak, arXiv:2402.03294.
- [21] K. Kang, Y. Qiu, K. Watanabe, T. Taniguchi, J. Shan,

- and K. F. Mak, arXiv:2402.04196.
- [22] E. Tang, J.-W. Mei, and X.-G. Wen, Phys. Rev. Lett. **106**, 236802 (2011).
- [23] K. Sun, Z. Gu, H. Katsura, and S. Das Sarm, Phys. Rev. Lett. **106**, 236803 (2011).
- [24] T. Neupert, L. Santos, C. Chamon, and C. Mudry, Phys. Rev. Lett. **106**, 236804 (2011).
- [25] N. Regnault and B. A. Bernevig, Phys. Rev. X **1**, 021014 (2011).
- [26] D. N. Sheng, Z.-C. Gu, K. Sun, and L. Sheng, Nat. Commun. **2**, 389 (2011).
- [27] K. L. Seyler, P. Rivera, H. Yu, N. P. Wilson, E. L. Ray, D. G. Mandrus, J. Yan, W. Yao, and X. Xu, Nature (London) **567**, 66 (2019).
- [28] K. Tran, *et al.* Nature (London) **567**, 71 (2019).
- [29] C. Jin, E. C. Regan, A. Yan, M. Iqbal Bakti Utama, D. Wang, S. Zhao, Y. Qin, S. Yang, Z. Zheng, S. Shi, K. Watanabe, T. Taniguchi, S. Tongay, A. Zettl, and F. Wang, Nature (London) **567**, 76 (2019).
- [30] E. M. Alexeev, D. A. Ruiz-Tijerina, M. Danovich, M. J. Hamer, D. J. Terry, P. K. Nayak, S. Ahn, S. Pak, J. Lee, J. I. Sohn, M. R. Molas, M. Koperski, K. Watanabe, T. Taniguchi, K. S. Novoselov, R. V. Gorbachev, H. S. Shin, V. I. Fal'ko, and A. I. Tartakovskii, Nature (London) **567**, 81 (2019).
- [31] E. Liu, E. Barré, J. van Baren, M. Wilson, T. Taniguchi, K. Watanabe, Y. T. Cui, N. M. Gabor, T. F. Heinz, Y. C. Chang, and C. H. Lui, Nature (London) **594**, 46 (2021).
- [32] Z. Zhang, E. C. Regan, D. Wang, W. Zhao, S. Wang, M. Sayyad, K. Yumigeta, K. Watanabe, T. Taniguchi, S. Tongay, M. Crommie, A. Zettl, M. P. Zaletel, and F. Wang, Nat. Phys. **18**, 1214 (2022).
- [33] L. Zhang, F. Wu, S. Hou, Z. Zhang, Y. H. Chou, K. Watanabe, T. Taniguchi, S. R. Forrest, and H. Deng, Nature (London) **591**, 61 (2021).
- [34] F. Wu, T. Lovorn, and A. H. MacDonald, Phys. Rev. Lett. **118**, 147401 (2017).
- [35] H. Yu, G.-B. Liu, J. Tang, X. Xu, and W. Yao, Sci. Adv. **3**, e1701696 (2017).
- [36] F. Wu, T. Lovorn, and A. H. MacDonald, Phys. Rev. B **97**, 035306 (2018).
- [37] H. Yu, Y. Wang, Q. Tong, X. Xu, and W. Yao, Phys. Rev. Lett. **115**, 187002 (2015).
- [38] H. Yu and W. Yao, Phys. Rev. X **11**, 021042 (2021).
- [39] R. Xiong, J. H. Nie, S. L. Brantly, P. Hays, R. Sailus, K. Watanabe, T. Taniguchi, S. Tongay, and C. Jin, Science **380**, 860 (2023).
- [40] H. Park, J. Zhu, X. Wang, Y. Wang, W. Holtzmann, T. Taniguchi, K. Watanabe, J. Yan, L. Fu, T. Cao, D. Xiao, D. R. Gamelin, H. Yu, W. Yao, and X. Xu, Nat. Phys. **19**, 1286 (2023).
- [41] B. Gao, D. G. Suárez-Forero, S. Sarkar, T.-S. Huang, D. Session, M. J. Mehrabad, R. Ni, M. Xie, J. Vannucci, S. Mittal, K. Watanabe, T. Taniguchi, A. Imamoglu, Y. Zhou, and M. Hafezi, Nat. Commun. **15**, 2305 (2024).
- [42] S. Miao, T. Wang, X. Huang, D. Chen, Z. Lian, C. Wang, M. Blei, T. Taniguchi, K. Watanabe, S. Tongay, Z. Wang, D. Xiao, Y.-T. Cui, and S.-F. Shi, Nat. Comm. **12**, 3608 (2021).
- [43] Z. Lian, Y. Meng, L. Ma, I. Maity, L. Yan, Q. Wu, X. Huang, D. Chen, X. Chen, X. Chen, M. Blei, T. Taniguchi, K. Watanabe, S. Tongay, J. Lischner, Y.-T. Cui, and S.-F. Shi, Nat. Phys. **20**, 34 (2024).
- [44] R. Xiong, S. L. Brantly, K. Su, J. H. Nie, Z. Zhang, R. Banerjee, H. Ruddick, K. Watanabe, T. Taniguchi, S. A. Tongay, C. Xu, and C. Jin, Nat. Commun. **15**, 4254 (2024).
- [45] For perfectly angle-aligned common chalcogen bilayers, the small lattice mismatch is accommodated by minimal strain between the two layers, resulting in a moiré-free interface [46–48].
- [46] J.-H. Baek, H. G. Kim, S. Y. Lim, S. C. Hong, Y. Chang, H. Ryu, Y. Jung, H. Jang, J. Kim, Y. Zhang, K. Watanabe, T. Taniguchi, P. Y. Huang, H. Cheong, M. Kim, and G.-H. Lee, Nat. Mater. **22**, 1463 (2023).
- [47] M. Förg, L. Colombier, R. K. Patel, J. Lindlau, A. D. Mohite, H. Yamaguchi, M. M. Glazov, D. Hunger, and A. Högele, Nat. Commun. **10**, 3697 (2019).
- [48] W.-T. Hsu, L.-S. Lu, P.-H. Wu, M.-H. Lee, P.-J. Chen, P.-Y. Wu, Y.-C. Chou, H.-T. Jeng, L.-J. Li, M.-W. Chu, and W.-H. Chang, Nat. Commun. **9**, 1356 (2018).
- [49] Twisted WSe₂ and MoTe₂ homobilayers are both experimentally verified examples which have a nontrivial topological interlayer hybridization. We chose the tWSe₂ as an example because the common chalcogen specie of MoTe₂, i.e., WTe₂, does not have a stable *R*-type crystal structure.
- [50] F. Wu, F. Qu, and A. H. MacDonald, Phys. Rev. B **91**, 075310 (2015).
- [51] H. Yu, G.-B. Liu, P. Gong, X. Xu, and Wang Yao, Nat. Commun. **5**, 3876 (2014).
- [52] D. Y. Qiu, T. Cao, and S. G. Louie Phys. Rev. Lett. **115**, 176801 (2015).
- [53] T. Cao, G. Wang, W. Han, H. Ye, C. Zhu, J. Shi, Q. Niu, P. Tan, E. Wang, B. Liu, and J. Feng, Nat. Commun. **3**, 887 (2012).
- [54] See Supplemental Material for details on the BSE calculation, the derivation of the exciton moiré Hamiltonian, and construction of Wannier orbitals and the effective lattice model, which includes Refs. [55, 56].
- [55] S. Larentis, H. C. P. Movva, B. Fallahzad, K. Kim, A. Behroozi, T. Taniguchi, K. Watanabe, S. K. Banerjee, and E. Tutuc, Large effective mass and interaction-enhanced Zeeman splitting of K-valley electrons in MoSe₂, Phys. Rev. B **97**, 201407(R) (2018).
- [56] B. A. Bernevig, Z.-D. Song, N. Regnault, and B. Lian, Twisted bilayer graphene. I. Matrix elements, approximations, perturbation theory, and a *k*·*p* two-band model, Phys. Rev. B **103**, 205411 (2021).
- [57] M. Röhlfing and S. G. Louie, Phys. Rev. B **62**, 4927 (2000).
- [58] F. Wu, T. Lovorn, E. Tutuc, and A. H. MacDonald, Phys. Rev. Lett. **121**, 026402 (2018)
- [59] F. Wu, T. Lovorn, E. Tutuc, I. Martin, and A. H. MacDonald, Phys. Rev. Lett. **122**, 086402 (2019).
- [60] H. Pan, F. Wu, and S. Das Sarma, Phys. Rev. Res. **2**, 033087 (2020)
- [61] T. Devakul, V. Crépel, Y. Zhang, and L. Fu, Nat. Commun. **12**, 6730 (2021).
- [62] H. Yu, M. Chen, and W. Yao, Nat. Sci. Rev., **7**, 12 (2020).
- [63] D. Zhai and W. Yao Phys. Rev. Mater. **4**, 094002 (2020).
- [64] N. Götting, F. Lohof, and C. Gies, Phys. Rev. B **105**, 165419 (2022).
- [65] X.-J. Luo, M. Wang, and F. Wu, Phys. Rev. B **107**, 235127 (2023).
- [66] F. D. M. Haldane, Phys. Rev. Lett. **61**, 2015 (1988).
- [67] C. L. Kane and E. J. Mele, Phys. Rev. Lett. **95**, 226801 (2005).

- [68] Y.-F. Wang, Z.-C. Gu, C.-D. Gong, and D. N. Sheng, Phys. Rev. Lett. **107**, 146803 (2011).
- [69] Y.-F. Wang, H. Yao, Z.-C. Gu, C.-D. Gong, and D. N. Sheng, Phys. Rev. Lett. **108**, 126805 (2012).
- [70] H. Li, Z. Xiang, M. H. Naik, W. Kim, Z. Li, R. Sailus, R. Banerjee, T. Taniguchi, K. Watanabe, S. Tongay, A. Zettl, F. H. da Jornada, S. G. Louie, M. F. Crommie, and F. Wang, Nat. Mater. **23**, 633 (2024).
- [71] E. Barré, O. Karni, E. Liu, A. L O’Beirne, X. Chen, H. B Ribeiro, L. Yu, B. Kim, K. Watanabe, T. Taniguchi, K. Barmak, C. H. Lui, S. Refaely-Abramson, F. H da Jornada, and F. F Heinz, Science **376**, 406 (2022).
- [72] M. Heiblum and D. E. Feldman, in *Fractional Quantum Hall Effects: New Developments*, 1st ed., edited by B. I. Halperin and J. K. Jain, (World Scientific, Singapore, 2020).
- [73] Y.-C. He, F. Grusdt, A. Kaufman, M. Greiner, and A. Vishwanath, Phys. Rev. B **96**, 201103(R) (2017).
- [74] M. Gerster, M. Rizzi, P. Silvi, M. Dalmonte, and S. Montanero, Fractional quantum Hall effect in the interacting Hofstadter model via tensor networks, Phys. Rev. B **96**, 195123 (2017).
- [75] P. Rosson, M. Lubasch, M. Kiffner, and D. Jaksch, Bosonic fractional quantum Hall states on a finite cylinder, Phys. Rev. A **99**, 033603 (2019).
- [76] Y. H. Kwan, Y. Hu, S. H. Simon, and S. A. Parameswaran, Phys. Rev. B **105**, 235121 (2022).
- [77] M. Xie and A. H. MacDonald, Phys. Rev. Lett. **121**, 067702 (2018).
- [78] L. Ma, P. X. Nguyen, Z. Wang, Y. Zeng, K. Watanabe, T. Taniguchi, A. H. MacDonald, K. F. Mak, and J. Shan, Strongly correlated excitonic insulator in atomic double layers, Nature (London) **598**, 585 (2021).
- [79] P. X. Nguyen, L. Ma, R. Chaturvedi, K. Watanabe, T. Taniguchi, J. Shan, and K. F. Mak, arXiv:2309.14940.
- [80] R. Qi, A. Y. Joe, Z. Zhang, J. Xie, Q. Feng, Z. Lu, Z. Wang, T. Taniguchi, K. Watanabe, S. Tongay, and F. Wang, arXiv:2309.15357.